A Comparative Study of Time Domain and Joint Time-Frequency Domain Methods for Ionospheric Irregularity Drift Velocity Estimation from a GNSS Receiver Array during High Latitude Ionospheric Scintillation

Jun Wang[1] and Yu Morton[1]

[1]Colorado State University
Engineering Room B104, 1373 Campus Delivery
Fort Collins, CO 80523-1373
United States of America

ABSTRACT

The spaced-receiver technique is an inexpensive approach for estimating the ionospheric irregularity drift velocity via an array of GNSS receivers during ionospheric scintillations. A closely spaced high-rate GNSS receiver array has been established for this purpose at Poker Flat, Alaska, where phase fluctuations are more frequent and intense than amplitude scintillations. When applying this approach to the array's carrier phase measurements, we have discovered that both the conventional time-domain method and a time-frequency-domain method are capable of estimating the irregularity drift via cross-correlation techniques, if the signal to noise ratio level is sufficiently high. In this study, both methods are applied to the Poker Flat GNSS array data collected during a prominent phase scintillation event on 2015/12/20. The results are compared and analysed to study the characteristic of each method. The estimated irregularity drift velocities are further cross-compared with the measurements from the PFISR.

1. INTRODUCTION

The fundamental theory of the spaced-receiver technique for estimating ionospheric irregularity drift velocity was developed by *Mitra* [1949] and *Briggs et al.* [1950; 1968]. The gist of the approach is to derive the time lag of scintillation signature across a closely spaced receiver array via time-domain cross-correlation. This technique has gained popularity with the advent of inexpensive global navigation satellite system (GNSS) receivers [*Vacchione et al.*, 1987; *Ledvina et al*., 2004].

The conventional approach focuses on the equatorial zonal drift velocity estimation from GPS L1 signal intensity measurements during amplitude scintillations [*Basu et al*., 1991; *Kil et al*., 2000]. At high latitudes, however, it is more suitable to use carrier phase measurements, since phase fluctuations are more frequent and intense than amplitude scintillations [*Aarons*, 1997; *Doherty et al*., 2003; *Skone et al.*, 2008; *Jiao et al*., 2013]. In our previous studies at Gakona, Alaska, the signal condition of GNSS carrier phase is not ideal for the conventional time-domain cross-correlation method. We proposed an alternative time-frequency-domain approach [*Wang and Morton*, 2015]. With our recent GNSS receiver array establishment at Poker Flat, Alaska, the signal condition has been greatly improved. We discovered that the time-domain technique can also resolve the time lag information across the receiver array [*Wang and Morton*, 2017].

The objective of this paper is to investigate the similarities/differences between the time-domain method (TDM) and the time-frequency domain method (TFDM). This comparative study is conducted upon the Poker Flat GNSS array data collected during a prominent phase scintillation event on 2015/12/20. The time lag results are compared and analysed to study the characteristic of

each method. The estimated drift velocities from each method are further cross-compared against the measurements from the co-located Poker Flat Incoherent Scatter Radar (PFISR).

The structure of this paper is as follows: In Section 2, the system setup of the GNSS receiver array is discussed in Section 2. Section 3 gives the overview of the methodologies to both the time-domain and the time-frequency-domain approaches. In Section 4, a comparative study is conducted on the estimated time lags from both methods. The estimated irregularities drift velocities are also cross-compared against the PFISR measurements. Section 5 gives the conclusion of this work.

2. SYSTEM SETUP

Since 2014, a GNSS receiver array has been established at the Poker Flat Research Range near Fairbanks, Alaska (65.13 °N, 147.49 °W). High quality multi-constellation GNSS receiver data has been continuously recorded for ionospheric scintillation monitoring. Having other co-located instruments for ionospheric observations such as the PFISR is one of the motivations to set up the GNSS array at this site. Detailed setup of the PFISR's is given by *Nicolls and Heinselman,* [2007]. Figure 1 shows the receiver array and data collection system arrangement scaled to the real geometry together with the PFISR's location.

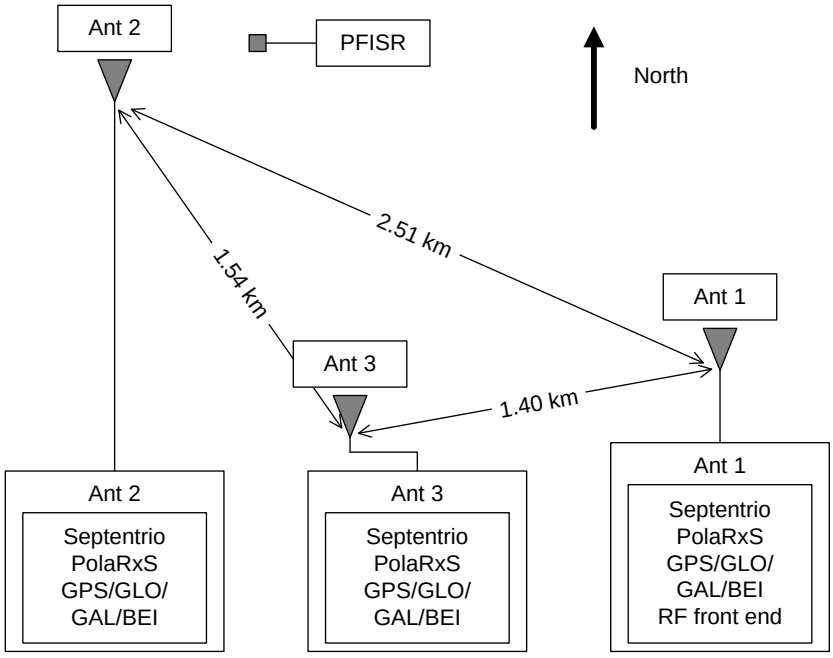

Figure 1. Poker Flat GNSS receiver array setup. The Antenna locations are marked by the triangles, while the PFISR location is marked by the square.

The PFISR is located 0.55 km east of Antenna 2. Each antenna is connected to a Septentrio PolaRxS ISM receiver, which is driven by a low phase noise, oven-controlled crystal oscillator and generates 100Hz GPS/GLONASS/Galileo/Beidou carrier phase measurements [*Taylor et al.*, 2013]. Antenna 1 signal is also split to a bank of software-defined multi-GNSS radio frequency front ends, then post-processed using custom developed receiver algorithms.

In order to understand the common measurement volume of the GNSS array and the PFISR, the sky coverages of both systems are shown by Figure 2. For the GNSS receiver array, its coverage is

illustrated by all GNSS satellite tracks observed from the array location using a full-day example on 2015/03/28. For the PFISR, its coverage is illustrated by all the possible look directions (Figure 1 in *Heinselman and Nicolls* [2008]).

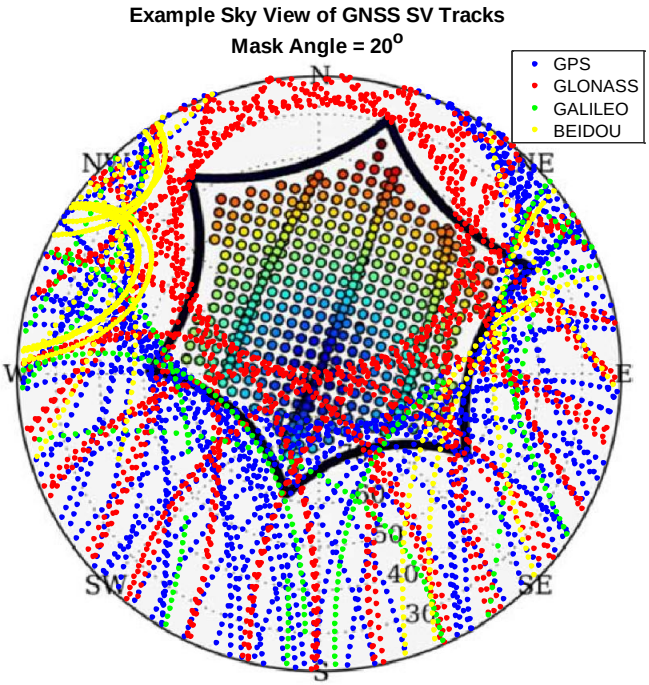

Figure 2. Sky coverages of the GNSS receiver array and the PFISR, expressed in a sky plot covering elevation angles from 20° to 90°. The GNSS array's coverage is illustrated by the colored dots (GPS, blue; GLONASS, red; Galielo, green; and Beidou, yellow), giving the satellite locations at a 5-minute resolution. The PFISR's coverage is illustrated by the star-shaped pattern in black, containing all the possible look directions (higher elevations, blue; lower elevations, red).

By comparing the sky coverages of the two systems, it can be observed that they have very limited common views of the sky. Most of the overlapping coverages are contributed by the GLONASS satellites. On one hand, this lack in overlapping areas limits direct point-to-point comparisons between the two systems. On the other hand, the two systems can be used to complement each other, especially when their combined view can almost cover the entire sky.

3. METHODOLOGIES

There are several data preprocessing steps necessary for subsequent drift velocity estimation methods, including receiver array data synchronization, cycle slip detection and repairing, and carrier phase data detrending. These preprocesses are documented in *Wang and Morton* [2015], and *Wang and Morton* [2017].

3.1 The Time-Domain Method

The TDM used in this study follows the conventional time-domain cross-correlation technique [*Kil et al*., 2000]. The only difference is that it is applied on GNSS carrier phase measurements instead of signal intensity measurements. During the process of acquiring the time shifts at correlation peaks (or time lags), the correlation coefficients are generated as by-products. Intuitively, correlation values associated with higher coefficients are desired, as they represent higher confidence levels. However, excessively high correlation coefficient thresholds lead to very few admissible time lag

estimations, degrading the statistical performance of the algorithm. By matching the GPS L1 estimated drift velocities with the GPS L2C estimations, *Wang and Morton* [2017] proposed a reasonably balanced correlation coefficient threshold at 70%, which is adopted in this study as well.

3.2 The Time-Frequency-Domain Method

In our previous studies, we have also demonstrated that it is feasible to use joint time-frequency analysis of GNSS carrier phase measurements to estimate irregularity drift [*Wang et al*., 2014; *Wang and Morton*, 2015]. The gist of the approach is to transform the original time-domain phase measurements into time-frequency-domain, so that the spectral features of the scintillation can be revealed. The basis of the TFDM is an adaptive periodogram technique (APT), which adaptively detect the optimal window length of any frequency component to produce high resolution time-frequency spectrum [*Wang and Morton,* 2015]. After the transformation, additional spectral filtering routines are applied to increase the signal-to-noise ratio of scintillation signatures. As a result, this method is especially suitable for weak signal conditions. A drawback of the TFDM is that it is more computationally expensive than the simple TDM.

3.3 The Comparison Scheme

The comparative study between the TDM and TFDM is conducted based on a real scintillation event occurred on 2015/12/20. The comparison is carried out from two aspects: the time lag estimations and the calculated drift velocities. First, the same carrier phase data are passed through both methods to produce the time lag estimations. The similarities and differences in these estimations are compared and analysed. The correlation coefficients generated in the calculations are also studied. Then, the drift velocities are calculated from both methods using a front velocity model [*Wang and Morton*, 2017]. After comparing these results, these drift velocity estimations are further cross-compared with the PFISR measurements to ensure the validity of the estimations.

4. COMPARISON AND ANALYSIS

4.1 The Scintillation Event

An intense geomagnetic storm event occurred during December 19-21, 2015. The main phase of this event was from ~1616 UT on 2015/12/19 (marked by the sudden storm commencement, SSC) to ~2300 UT on 2015/12/20 (marked by the maximum intensity Dst index at -155 nT) [Ebre Observatory, http://www.obsebre.es/en/rapid; WDC Kyoto Observatory, http://wdc.kugi.kyoto-u.ac.jp/wdc/Sec3.html]. More details describing this event can be found in *Wang and Morton* [2017]. The specific data period selected during this event is from 1600UT to 1800UT on 2015/12/20, which was right after the Auroral Electroject (AE) index reached maximum value at 1883 nT. During this two-hour period, the global geomagnetic Kp index stayed at 7.

The GNSS signal chosen to be analysed is the GPS L1 signal. This is because very few Galileo and Beidou satellites are above 30° elevations during this period, while the GLONASS signal quality is inferior to that of GPS due to satellite clock noise. There are 9 GPS satellites occurred above 30° elevations during this two-hour period, including PRN 8, 10, 15, 16, 18, 20, 21, 26 and 27.

4.2 Time Lag Comparison

Time lag estimations are generated for both methods, together with their corresponding correlation coefficients. An example of the correlation results is given between antenna pairs 1 and 2. 5 out of

the 9 GPS satellites are mostly visible within this two-hour period, including PRN 16, 18, 20, 21 and 27. The time lag and correlation coefficient results are plotted in Figure 3 for both methods.

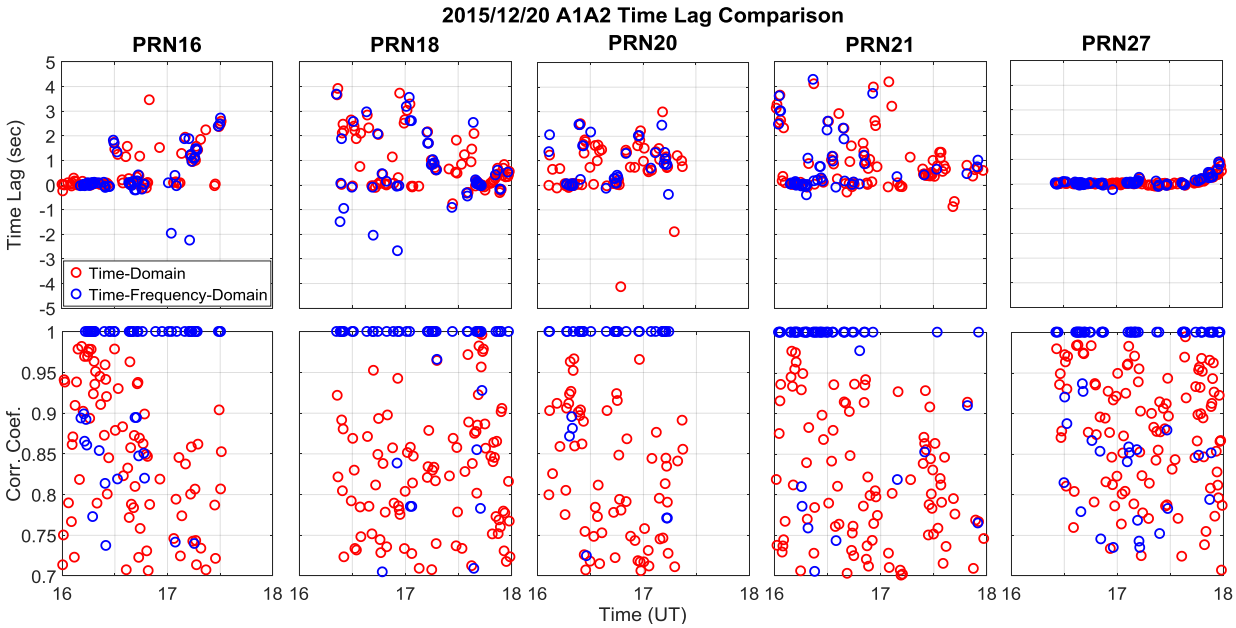

Figure 3. Example of time lag comparison between the two methods on A1-A2 antenna pair. The time lags are given in the top row while their corresponding correlation coefficients are in the bottom row. For left to right, results for PRN 16, 18, 20, 21 and 27 are plotted. The red circles represent results for the TDM while the blue circles represent results for the TFDM.

In the top row of Figure 3, time lags of the TFDM agree well with the results of the TDM. Most of the time lag results are above zero, implying that the drift velocity direction is consistent along the A1-A2 pair for these satellites. Several negative lags do exist for both methods, which are likely to be outliers. As for the correlation coefficient results in the bottom row, the values for the TFDM is notably higher than those of the TDM. This is because of spectral filtering in the TFDM, which reduces noise contributions.

To quantitatively characterize the difference between the calculated time lags for each method, mean values and standard deviations of the time lag\differences are calculated. The statistical performance for each GPS satellite across each antenna pair is captured by Table 1 as follows:

Table 1. Mean values and standard deviations of the time lag differences between the two methods.

(in seconds)	PRN8	PRN10	PRN15	PRN16	PRN18	PRN20	PRN21	PRN26	PRN27
A1A2 mean	-0.13	0.27	2.25	0.03	0.10	0.28	-0.74	0.21	0.03
A1A2 std	0.24	0.93	3.82	0.15	1.77	1.29	2.57	1.02	0.12
A1A3 mean	-0.11	N/A	0.16	0.04	-0.27	0.002	0.18	-0.03	-0.06
A1A3 std	0	N/A	0.67	0.17	0.86	0.47	1.17	0.37	0.25
A2A3 mean	0.06	N/A	-0.01	-0.17	-0.06	0.45	-0.06	0.91	0.19
A2A3 std	0.18	N/A	0.27	0.75	0.33	2.07	2.58	2.22	1.16

.

In Table 1, some values on PRN10 are missing due to a data recording issues on antenna 3. Other than that, the time lag differences between the two methods along any antenna pair are fairly small. Note that the overall differences along Antennas 1 and 3 are smaller than those of the other two

antenna pairs. This is likely due to the fact that the physical distance between these two antennas is the smallest among all antenna pairs.

4.3 Drift Velocity Comparison

The ionospheric drift velocities are calculated for each method using the front velocity model. These velocities are then converted from the local East-North-Up coordinate system into the geomagnetic coordinate system to match PFISR's vector velocity format [*Heinselman and Nicolls*, 2008]. The mean values and the standard deviations of the estimated velocities are produced every 5 minutes. The TDM and the TFDM are compared based on their drift velocity estimations. The comparison result is captured by Figure 4, with the PFISR measurements in the background as references.

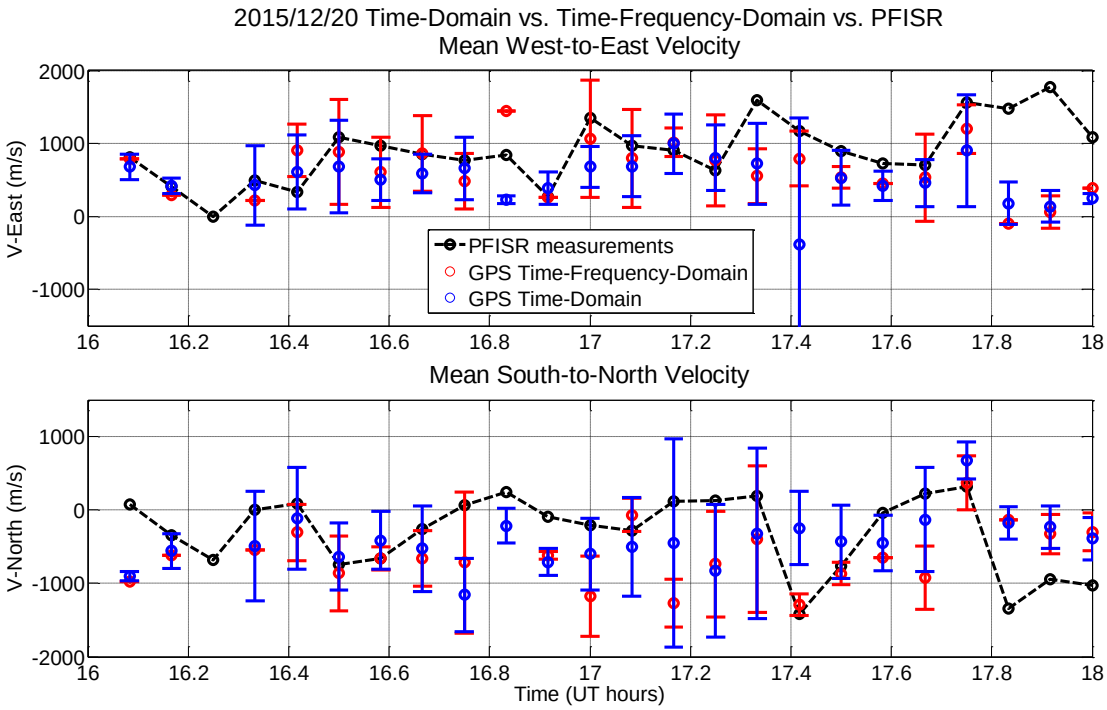

Figure 4. Drift velocity comparison between the TDM (blue) and the TFDM (red), with measurements from the PFISR (black, dashed) in the background. The mean values of the estimated velocities are represented by the circles, with the error bars indicating the standard deviations. The top panel represents results in the geomagnetic west-to-east direction while the bottom panel represents the geomagnetic south-to-north direction.

In Figure 4, red and blue circles are often very close to each other, showing a good agreement between the two methods in terms of the estimation mean. Meanwhile, the red error bars are often contained in the blue counterparts, suggesting that the TFDM has better consistency and reliability over the TDM.

Comparing these estimation results against the reference values measured by the PFISR, the black circles are often within the error bar boundaries, showing favorable agreements between the two systems. Exceptions can be found towards the end of the data. Also, note that the estimated west-to-east velocities demonstrate better agreement with the PFISR measurements than velocities in the south-to-north direction. This is likely due to the larger longitudinal spread of the GNSS array arrangement than its latitudinal spread.

5. CONCLUSION

In this paper, the TDM and the TFDM for ionospheric drift velocity estimation using spaced GNSS receivers are compared and analysed based on a case study during high latitude phase scintillation on 2015/12/20. Overall, the two methods demonstrate good agreement, in terms of both time lag estimations and resulting drift velocity estimations. The TFDM exhibits slightly better consistency and reliability over the TDM. This is an expected outcome, since the spectral filtering processes in the TFDM can reveal the fine features of the scintillation event.

The two estimation methods are then compared favourably against the measurements from the PFISR. Note that the mechanism and the spatial coverage of the two systems are very different.

ACKNOWLEDGEMENTS

This project is supported by a grant from AFOSR (FA9550-14-1-0265). The GNSS data used in this study is collected with the help of members of Colorado State University GPS Lab, Harrison Bourne and Steve Taylor. We acknowledge the Madrigal database (http://isr.sri.com/madrigal) for providing the AMISR data. The Poker Flat Incoherent Scatter Radar is operated by SRI International on behalf of the US National Science Foundation under NSF Cooperative Agreement AGS-1133009. We thank the World Data Center for Geomagnetism operated by the Kyoto University (http://wdc.kugi.kyoto-u.ac.jp) for providing the Kp, AE and Dst indices. The SSC information is available from the Ebre Observatory (http://www.obsebre.es/en/rapid), entrusted by the International Association of Geomagnetism and Aeronomy (IAGA). The authors also wish to thank Dr. Don Hampton at the University of Alaska Fairbanks and staff at Poker Flat for hosting the GNSS array.

REFERENCES

Aarons, J. (1997). Global positioning system phase fluctuations at auroral latitudes. *Journal of Geophysical Research: Space Physics (1978–2012)*, 102(A8), 17219-17231.

Basu, S., Basu, S., Kuoeki, E., Zengingonul, H. P., Biondi, M. A., and Meriwether, J. W. (1991). Zonal irregularity drifts and neutral winds measured near the magnetic equator in Peru. *Journal of Atmospheric and Terrestrial Physics*, *53*(8), 743-755

Briggs, B. H., Phillips, G. J., and Shinn, D. H. (1950). The analysis of observations on spaced receivers of the fading of radio signals. *Proceedings of the Physical Society. Section B*, *63*(2), 106

Briggs, B. H. (1968). On the analysis of moving patterns in geophysics—I. Correlation analysis. *Journal of Atmospheric and Terrestrial Physics*, *30*(10), 1777-1788

Doherty, P. H., Delay, S. H., Valladares, C. E., and Klobuchar, J. A. (2003). Ionospheric scintillation effects on GPS in the equatorial and auroral regions. *Navigation*, *50*(4), 235-245

Heinselman, C. J., and Nicolls, M. J. (2008). A Bayesian approach to electric field and E-region neutral wind estimation with the Poker Flat Advanced Modular Incoherent Scatter Radar. *Radio Science*, *43*(5)

Kil, H., Kintner, P. M., Paula, E. R., and Kantor, I. J. (2000). Global Positioning System measurements of the ionospheric zonal apparent velocity at Cachoeira Paulista in Brazil. *Journal of Geophysical Research: Space Physics (1978–2012)*, *105*(A3), 5317-5327

Jiao, Y., Morton, Y. T., Taylor, S., and Pelgrum, W. (2013). Characterization of high-latitude ionospheric scintillation of GPS signals. *Radio Science*, 48(6), 698-708

Ledvina, B. M., Kintner, P. M., and de Paula, E. R. (2004). Understanding spaced-receiver zonal velocity estimation. *Journal of geophysical research*,*109*(A10), A10306

Mitra, S. N. (1949). A radio method of measuring winds in the ionosphere. *Proceedings of the IEE-Part III: Radio and Communication Engineering*, *96*(43), 441-446

Nicolls, M. J., and C. J. Heinselman (2007), Three-dimensional measurements of traveling ionospheric disturbances with the Poker Flat Incoherent Scatter Radar, *Geophys. Res. Lett.*, 34, L21104, doi:10.1029/2007GL031506

Skone, S., Man, F., Ghafoori, F., and Tiwari, R. (2008). Investigation of scintillation characteristics for high latitude phenomena. *Proc. ION GNSS*, Savana, GA

Taylor, S., Marcus, R.J., Bourne, H., Morton, Y., and Pelgrum, W. (2013). Ionosphere scintillation receiver performances based on high latitude experiments. *Proc. ION Pacific PNT*, Honolulu, HI

Vacchione, J. D., Franke, S. J., and Yeh, K. C. (1987). A new analysis technique for estimating zonal irregularity drifts and variability in the equatorial F region using spaced receiver scintillation data. *Radio science*, *22*(5), 745-756

Wang, J., and Morton, Y. T. (2015). High-Latitude Ionospheric Irregularity Drift Velocity Estimation Using Spaced GPS Receiver Carrier Phase Time–Frequency Analysis. *IEEE Transactions on Geoscience and Remote Sensing*, *53*(11), 6099-6113

Wang, J., and Morton, Y. T. (2017). A Comparative Study of Ionospheric Irregularity Drift Velocity Derived from a GNSS Receiver Array and PFISR Measurements during High Latitude Ionospheric Scintillation. Submitted to *Journal of Geophysical Research - Space Physics*.